



## Article

## The Assembly of Grid-type Lanthanide Cluster

Jinsong Li <sup>1</sup>, Fan Zhang <sup>1</sup>, Xuefeng Guo <sup>2</sup>, Dan Liu <sup>2,\*</sup> and Jianfeng Wu <sup>1,\*</sup><sup>1</sup> School of Chemistry and Chemical Engineering, Northwestern Polytechnical University, Xi'an 710072, China<sup>2</sup> Institute of Flexible Electronics (IFE), Northwestern Polytechnical University, Xi'an 710072, China

\* Correspondence: iamdliu@nwpu.edu.cn (D.L.); jf.wu.chem@gmail.com (J.W.)

**Abstract:** A dicompartmental Schiff base ligand was synthesized and used for the assembly of a lanthanide grid-like complex. Dinuclear **Dy**<sub>2</sub> and tetranuclear **Dy**<sub>4</sub> complexes were isolated from the reaction of the ligand with different dysprosium salt. Single crystal X-ray diffractions show that the two Dy<sup>III</sup> ions in **Dy**<sub>2</sub> are adopted in the N<sub>3</sub>O coordination pockets of the ligand and further coordinated by water molecules, whereas, for **Dy**<sub>4</sub>, the four Dy<sup>III</sup> ions are clamped by four ligands through their terminal N<sub>3</sub>O coordination pockets, forming a grid-type assembly. Magnetic studies reveal that complex **Dy**<sub>2</sub> shows field-induced single-molecule magnetic behavior under 1000 Oe dc field, complex **Dy**<sub>4</sub> shows fast relaxation under zero field and field-induced single-molecule magnet (SMM) behavior under 500 Oe. The difference in the magnetic relaxation is related to the various deprotonation of the ligand and distinct topology of the assemblies.

**Keywords:** lanthanide complex; grid topology; field-induced SMM; QTM

## 1. Introduction

Lanthanides single-molecule magnets (Ln-SMMs) have attracted much attention since the first discovery of (Bu<sub>4</sub>N)[Tb(Pc)<sub>2</sub>] [1], which shows record energy barriers and different relaxation mechanisms from that of the transition-metal-cluster SMMs. Since then, lanthanide has become the best candidate for the design and synthesis of high-performance SMMs [2–5] due to its potential applications in high-density information storage, quantum information processing [6], and molecular spintronic materials [7–12]. During the last two decades, thousands of Ln-SMM have been reported, and the record energy barrier ( $U_{\text{eff}}$ ) and blocking temperature ( $T_B$ ) were refreshed up to 1541 cm<sup>−1</sup> and 80 K [13] respectively, pushing the potential application of SMMs into reality. However, due to the presence of fast quantum tunneling of magnetization (QTM), the relaxations of magnetizations in most of the reported SMMs are short cut, resulting in a relatively low blocking temperature [14–16].

One efficient way for suppressing QTM in Ln-SMM is restricting the lanthanide ions in an axial ligand field, such as  $C_{\infty v}$  [17,18],  $D_{4d}$  [19–22],  $D_{5h}$  [23–25], and  $D_{6d}$  coordination geometries for Dy<sup>III</sup> ions. Due to the inherent high coordination number and flexible coordination nature of lanthanide ions, it is very difficult and challenging to fix the lanthanide ions in a perfect due coordination geometry. Alternatively, introducing magnetic interaction between lanthanide ions can suppress the QTM efficiently [26], especially in polynuclear SMMs. For instance, the reported single-electron Ln–Ln coupling in dimetallofullerenes shows very strong exchange interactions between 4f moments that result in a gigantic coercivity of 8.2 teslas at 5 K and blocking temperature up to 25.2 K [27–29]. Long and co-workers reported a mixed-valence dilanthanide complexes (Cp<sub>2</sub>Pr<sub>5</sub>)<sub>2</sub>Dy<sub>2</sub>I<sub>3</sub> that gives rise to an enormous coercive magnetic field with a lower bound of 14 tesla up to 60 K [30]. Additionally, high-performance polynuclear SMMs are also found in radical [31–33] and  $\mu_2$ -OH<sup>−</sup> bridged [34–36] dinuclear lanthanide complexes, in which the spin centers are in axial ligand field and strongly coupled, suppressing the QTM efficiently. For Ln-SMMs with higher nuclearity, the poor axial ligand field, as well as the complicated topology of



**Citation:** Li, J.; Zhang, F.; Guo, X.; Liu, D.; Wu, J. The Assembly of Grid-type Lanthanide Cluster.

*Magnetochimistry* **2023**, *9*, 4.

<https://doi.org/10.3390/magnetochimistry9010004>

<https://doi.org/10.3390/magnetochimistry9010004>

Academic Editor: Andrea Cornia

Received: 20 November 2022

Revised: 20 December 2022

Accepted: 21 December 2022

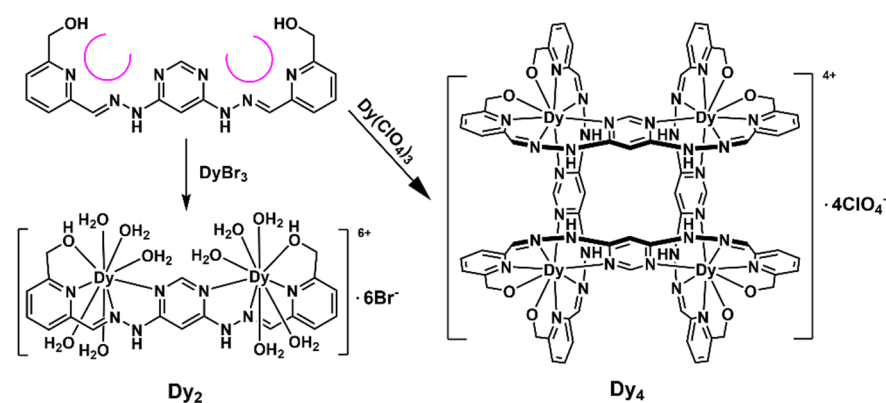
Published: 24 December 2022



**Copyright:** © 2022 by the authors. Licensee MDPI, Basel, Switzerland. This article is an open access article distributed under the terms and conditions of the Creative Commons Attribution (CC BY) license (<https://creativecommons.org/licenses/by/4.0/>).

the molecule, make it difficult to manipulate the relaxation processes and suppress the QTM [37–39].

Our research interests are focused on the unique magnetic behavior [40] in grid-type lanthanide assemblies, in which the QTM could be suppressed by the magnetic interaction between lanthanide ions [41]. For this, we have designed several types of ditopic and tritopic hydrazone ligands with suitable coordination pockets to accommodate lanthanide ions and arrange them in a grid [42–44] or hexagonal [45–47] topology. Herein, the linkers in the ligands are very important for the transmission of intermolecular magnetic interactions. As was reported in the literature, pyrimidine is a good linker to arrange transition metal ions into grid-type topologies [48–52]. However, the assembly of lanthanide grids based on pyrimidine ligands is rare [53]. Herein, we designed a pyrimidine-based dicompartmental Schiff base ligand with a pyrimidine linker, by using which a dinuclear  $\text{Dy}_2$  was isolated (Scheme 1). After optimizing the reaction conditions, tetranuclear  $\text{Dy}_4$  featuring a  $[2 \times 2]$  grid topology was also obtained. The magnetic study revealed that complex  $\text{Dy}_2$  shows field-induced single-molecule magnetic behavior under a 1000 Oe dc field.  $\text{Dy}_4$  shows fast relaxation under zero field, which was slowed down by the application of 500 Oe, resulting in the field-induced single-molecule magnet.



**Scheme 1.** Schematic drawing of the assemblies of complexes  $\text{Dy}_2$  and  $\text{Dy}_4$  from the dicompartmental Schiff base ligand.

## 2. Materials and Methods

### 2.1. Synthesis of Ligand $\text{H}_2\text{L}$

A 100-mL flask was charged with a magnetic stirrer bar and 4,6-dihydrazineylpyrimidine [54] (1.4 g, 10 mmol, 1 eq) in 50 mL methanol. 6-(hydroxymethyl)-2-carbaldehyde-pyridine [55] (2.74 g, 20 mmol, 2 eq) was then added. The reaction was stirred and refluxed overnight. Upon cooling, the precipitate was filtered, washed with ether, and dried under vacuum, giving the pure product  $\text{H}_2\text{L}$  (((pyrimidine-4,6-diylbis(hydrazin-2-yl-1-ylidene))bis(methaneylylidene))bis(pyridine-6,2-diyl))dimethanol) as a pale yellow powder. Yield: 3.1 g (82%). Elemental analysis (%) calcd for  $\text{C}_{18}\text{H}_{18}\text{N}_8\text{O}_2$ , MW = 378.16: C, 57.14, H, 4.79, N, 29.61; found C, 57.28, H, 4.81, N, 29.65.  $^1\text{H}$  NMR (500 MHz,  $\text{DMSO}-d_6$ )  $\delta$  = 11.43 (2 H, s), 8.24 (1 H, d, J 0.9), 8.14 (2 H, s), 7.93–7.85 (4 H, m), 7.46 (2 H, d, J 7.3), 6.94 (1 H, s), 5.47 (2 H, d, J 6.0), 4.62–4.58 (4 H, m). IR (KBr disks)  $\tilde{\nu}$  [ $\text{cm}^{-1}$ ] = 3394 (w), 3190 (m), 3047 (w), 1608 (s), 1585 (s), 1562 (s), 1504 (m), 1462 (m), 1421 (m), 1375 (m), 1323 (m), 1255 (m), 1198 (m), 1134 (s), 1084 (m), 993 (m), 916 (w), 833 (s), 746 (s), 719 (m), 651 (m), 624 (w), 561 (w), 501 (w) 463 (w).

### 2.2. Synthesis of $\text{Dy}_2$

$\text{DyBr}_3 \cdot 9\text{H}_2\text{O}$  (0.6 mmol) and ligand  $\text{H}_2\text{L}$  (0.2 mmol) in a mixture of 10 mL methanol and 5 mL DCM was stirred at room temperature for 10 min. The reaction was stirred at room temperature overnight. The solution was filtered and exposed to air to allow the slow evaporation of the solvent. Yellow crystals of  $\text{Dy}_2$  suitable for X-ray diffraction were

obtained after 4 days. Yield: 90 mg, (32%, based on metal salt). Elemental analysis (%) calcd for  $[\text{Dy}_2(\text{H}_2\text{L})(\text{H}_2\text{O})_{10}]\cdot\text{Br}_6\cdot 3\text{H}_2\text{O}$  ( $\text{C}_{18}\text{H}_{44}\text{Br}_6\text{Dy}_2\text{N}_8\text{O}_{15}$ , MW = 1417.07): C, 15.26, H, 3.14, N, 7.91; found C, 15.28, H, 3.11, N, 7.85. IR (KBr disks)  $\tilde{\nu}$  [ $\text{cm}^{-1}$ ] = 3336 (br, w), 3207 (br, w), 3060 (br, w), 1635 (s), 1610 (s), 1568 (m), 1531 (w), 1514 (w), 1487 (m), 1456 (m), 1410 (w), 1290 (m), 1221 (w), 1188 (s), 1146 (m), 1101 (w), 1049 (w), 1012 (w), 827 (w), 740 (w), 696 (w), 655 (w), 605 (w), 567 (w), 544 (m), 501 (w), 476 (m), 459 (w), 447 (w).

### 2.3. Synthesis of **Dy<sub>4</sub>**

A mixture of  $\text{Dy}(\text{ClO}_4)_3\cdot 6\text{H}_2\text{O}$  (0.3 mmol) and ligand **H<sub>2</sub>L** (0.2 mmol) in a mixture of 10 mL methanol and 5 mL DCM was stirred at room temperature for 10 min, triethylamine (0.2 mmol) was then added dropwise. The reaction was stirred at room temperature overnight. The solution was filtered and exposed to air to allow the slow evaporation of the solvent. Yellow crystals of **Dy<sub>4</sub>** suitable for X-ray diffraction were obtained after 5 days. Yield: 97 mg (65%, based on metal salt). Elemental analysis (%) calcd for  $[\text{Dy}_4\text{L}_4]\cdot(\text{ClO}_4)_4\cdot 12\text{MeOH}\cdot 4\text{H}_2\text{O}$  ( $\text{C}_{84}\text{H}_{120}\text{Cl}_4\text{Dy}_4\text{N}_{32}\text{O}_{40}$ , MW = 3009.91): C, 33.52, H, 4.02, N, 14.89; found C, 33.49, H, 4.03, N, 14.78. IR (KBr disks)  $\tilde{\nu}$  [ $\text{cm}^{-1}$ ] = 3456 (br, w), 3343 (br, w), 3016 (br, w), 2981 (br, w), 1635 (s), 1606 (s), 1558 (m), 1533 (m), 1477 (s), 1417 (m), 1375 (w), 1297 (m), 1223 (w), 1193 (s), 1145 (w), 1101 (s), 1036 (w), 1006 (w), 898 (w), 771 (w), 654 (w), 625 (m), 597 (w), 578 (w), 525 (w), 501 (w), 469 (w).

### 2.4. Crystallography

Single-crystal X-ray diffraction data were collected by the Bruker Apex II CCD diffractometer (Bruker AXS GMBH, Germany), using graphite-monochromatized Mo-K $\alpha$  radiation ( $\lambda = 0.71073$  Å). In the Olex2 package [56], the structures were solved by using SHELXT [57] (direct methods), and all non-hydrogen atoms were refined by using SHELXL [58] (full-matrix least-squares techniques) on *F*<sup>2</sup> with anisotropic thermal parameters. All hydrogen atoms were introduced in calculated positions and refined with fixed geometry relative to their carrier atoms. The solvent voids (164.1 Å<sup>3</sup> and 14.1 e<sup>−</sup> per cell) in **Dy<sub>4</sub>** were refined using a solvent masking routine in the Olex2 package. Due to the poor diffraction of **Dy<sub>4</sub>**, it is difficult to introduce hydrogen atoms on some of the solvent molecules in the lattice. Crystallographic data of **Dy<sub>2</sub>** and **Dy<sub>4</sub>** are listed in Table S1. CCDC 2220302 and 2220303 contain supplementary crystallographic data for this paper.

### 2.5. Magnetic Measurements

Magnetic measurements were performed by using a Quantum Design MPMS-XL-7 SQUID magnetometer (Quantum Design, United States) equipped with a 7 T magnet. Susceptibility measurements were carried out on the polycrystalline sample of the two complexes. In the temperature range of 2–300 K, the direct-current (dc) susceptibility measurements were obtained under an applied field of 1000 Oe. Diamagnetic corrections were made with Pascal's constants [59] for all the constituent atoms and the contributions of the sample holder. The field-dependent magnetizations were obtained in the field range of 0–7 T. In the frequency range of 1–1488 Hz, the alternating-current (ac) susceptibility measurements were obtained in a 3 Oe ac oscillating field under various dc fields.

## 3. Results and Discussions

### 3.1. Structures of **Dy<sub>2</sub>** and **Dy<sub>4</sub>**

The ligand **H<sub>2</sub>L** (((pyrimidine-4,6-diylbis(hydrazin-2-yl-1-ylidene)) bis(methaneylylidene))bis(pyridine-6,2-diyl))dimethanol) was synthesized from the condensation of 4,6-dihydrazineylpyrimidine and 6-(hydroxymethyl)-2-carbaldehyde-pyridine in good yield (Figure S1). As shown in Scheme 1, two four-membered O-N-N-N pockets reside at both sides of the ligand, which can capture two Dy<sup>III</sup> ions in a planar arrangement. Indeed, a dinuclear **Dy<sub>2</sub>**, with formula of  $[\text{Dy}_2(\text{H}_2\text{L})(\text{H}_2\text{O})_{10}]\cdot\text{Br}_6\cdot 3\text{H}_2\text{O}$ , was obtained from the reaction of  $\text{DyBr}_3\cdot 9\text{H}_2\text{O}$  (0.6 mmol) and ligand **H<sub>2</sub>L**. Yellow crystals of **Dy<sub>2</sub>** suitable for X-ray diffraction were obtained after the workup. Single-crystal X-ray diffraction revealed

that complex **Dy<sub>2</sub>** crystallizes in the triclinic space group *P*-1 with *Z* = 2 (Table S1). The asymmetric unit contains one ligand, two Dy<sup>III</sup> ions, ten coordinated water, six free Br<sup>−</sup>, and three water molecules in the lattice. The ligand is not deprotonated and coordinates with the Dy<sup>III</sup> ions by its coordination pockets on both sides (Figure 1a). **Dy<sub>1</sub>** and **Dy<sub>2</sub>** reside in the four-membered O-N-N-N pocket, with each further coordinated with five H<sub>2</sub>O molecules, forming a nine-coordination environment (O<sub>6</sub>N<sub>3</sub>). The Dy-O bonds are in the range of 2.37–2.46 Å, which is much shorter than the Dy-N bond (2.50–2.57 Å, Table S1), probably because of the hard-base behavior of the coordinated O atoms. The Dy<sup>III</sup> ions in the molecule are separated by the pyrimidine group with a distance of 6.67 Å. The Br<sup>−</sup> anions reside in the lattice to balance the positive charge of the molecule and form hydrogen bondings with the coordinated and free H<sub>2</sub>O, bridging the molecules into three-dimensional frameworks (Figure S6).

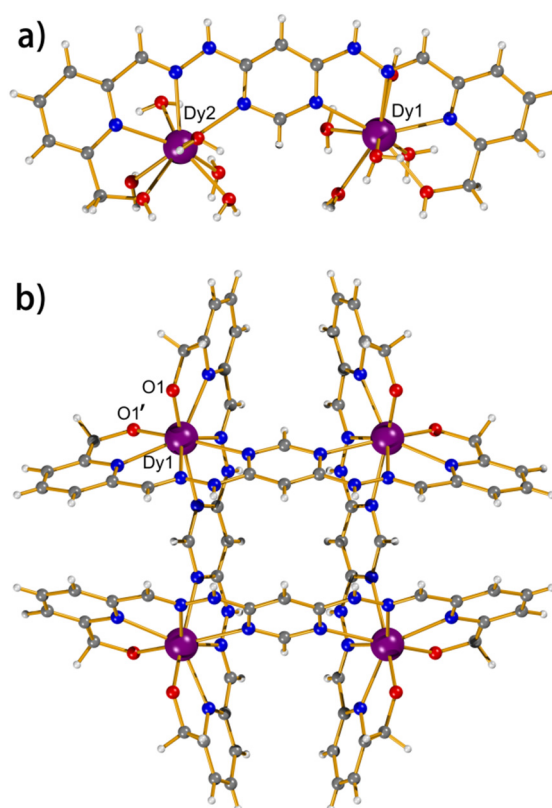


**Figure 1.** Structures of complexes **Dy<sub>2</sub>** (a) and **Dy<sub>4</sub>** (b). The cations and solvents have been omitted for clarity.

After adjusting the ligand–metal ratio and reaction conditions, fortunately, a tetranuclear grid-like complex **Dy<sub>4</sub>** ([Dy<sub>4</sub>L<sub>4</sub>](ClO<sub>4</sub>)<sub>4</sub>·12MeOH·4H<sub>2</sub>O) was isolated. Single crystal X-ray diffraction shows that complex **Dy<sub>4</sub>** crystallizes in the tetragonal space group *P*4<sub>2</sub>/*nmc* with *Z* = 2. The molecule contains four double deprotonated ligands, four Dy<sup>III</sup> ions, four perchlorate, and some solvent molecules (MeOH and H<sub>2</sub>O) in the lattice. The molecule features a [2 × 2] grid topology with the four ligands as the edges and four Dy<sup>III</sup> ions bending in the corners (Figure 1b). Due to the high symmetry of the molecule, all the Dy<sup>III</sup> ions and ligands are identical, with each Dy<sup>III</sup> ion clamped by two N<sub>3</sub>O coordination pockets from two crossed ligands, forming an eight-coordination environment. The ligands are deprotonated on both hydroxymethyl group sites, resulting in relatively short Dy-O bonds (2.27 Å), which is also much shorter than that of in complex **Dy<sub>2</sub>** (Dy-O > 2.39 Å). The shortest intramolecular Dy···Dy distance is 6.9 Å longer than that of **Dy<sub>2</sub>** (6.67 Å). This can be ascribed to the deprotonation of the hydroxymethyl groups that drag the Dy<sup>III</sup> ions close to the terminal sites of the ligand. The long Dy···Dy distance suggests the

weak or negligible magnetic exchange interaction within the complex. The molecules pack along the crystallographic C axis and are separated by the  $\text{ClO}_4^-$  and solvent molecules in the lattice.

To gain more insight into the coordination difference of  $\text{Dy}^{\text{III}}$  ions in the two complexes, the coordination geometries of the  $\text{Dy}^{\text{III}}$  centers were quantified by the SHAPE analyses [60,61]. As shown in Figure S8, the  $\text{Dy}^{\text{III}}$  ions in **Dy**<sub>2</sub> are both nine coordinated, and the coordination geometry of Dy1 and Dy2 in **Dy**<sub>2</sub> are close to Muffin ( $C_s$ ) with CShM value of 1.369 and capped square antiprism ( $C_{4v}$ ) with CShM value of 0.743 (Table S4), respectively. In **Dy**<sub>4</sub>, the four  $\text{Dy}^{\text{III}}$  ions are identical, and eight are coordinated in an  $\text{N}_6\text{O}_2$  coordination environment, the coordination geometry for Dy1 in a large distorted augmented trigonal prism ( $C_{2v}$ ) with a CShM value of 3.284. The difference in the coordinate geometry of the  $\text{Dy}^{\text{III}}$  ions in **Dy**<sub>2</sub> and **Dy**<sub>4</sub> will influence the magnetic relaxation significantly (see below).

### 3.2. Magnetic Properties of **Dy**<sub>2</sub> and **Dy**<sub>4</sub>

#### 3.2.1. Static Magnetic Properties of **Dy**<sub>2</sub> and **Dy**<sub>4</sub>

Direct current (dc) magnetic susceptibility measurements were carried out on polycrystalline samples under an applied field of 1000 Oe in the temperature range of 2–300 K. As shown in Figure 2, the temperature-dependent  $\chi_M T$  product ( $\chi_M$  = molar magnetic susceptibility) of the two complexes show similar profiles. The  $\chi_M T$  at 300 K are 27.44 and 53.39  $\text{cm}^3 \cdot \text{K} \cdot \text{mol}^{-1}$  for **Dy**<sub>2</sub> and **Dy**<sub>4</sub>, respectively, which are close to the expected value for two (28.34  $\text{cm}^3 \cdot \text{K} \cdot \text{mol}^{-1}$ ) and four (56.68  $\text{cm}^3 \cdot \text{K} \cdot \text{mol}^{-1}$ ) free-ion approximation of  $\text{Dy}^{\text{III}}$  ions ( $S = 5/2$ ,  $L = 5$ ,  $^6H_{15/2}$ ,  $g = 4/3$ ). Upon cooling, the  $\chi_M T$  products decrease gradually before a quick drop below 10 K and reach the value of 17.78  $\text{cm}^3 \cdot \text{K} \cdot \text{mol}^{-1}$  (**Dy**<sub>2</sub>) and 40.41  $\text{cm}^3 \cdot \text{K} \cdot \text{mol}^{-1}$  (**Dy**<sub>4</sub>) at 2 K. The quick drop of the  $\chi_M T$  products at low temperatures can be ascribed to the thermal depopulation of the Stark sublevels as well as the possibility of dominated weak antiferromagnetic interaction between the  $\text{Dy}^{\text{III}}$  ions.

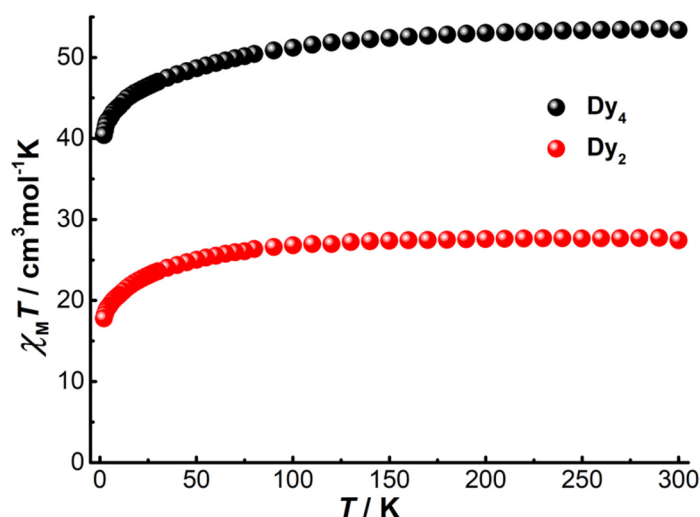


**Figure 2.** Temperature-dependent  $\chi_M T$  products at 1 kOe between 2 and 300 K for **Dy**<sub>2</sub> and **Dy**<sub>4</sub>.

The field-dependent molar magnetizations ( $M$ ) *vs.*  $H$  plot for **Dy**<sub>2</sub> and **Dy**<sub>4</sub> at 1.9 K (Figures S10 and S11) shows a sharp increase at low fields and then linear increases at high fields, reaching the values of 10.68  $\mu_B$  (**Dy**<sub>2</sub>) and 19.85  $\mu_B$  (**Dy**<sub>4</sub>) at 7 T, which are close to the expected value for two (10  $\mu_B$ ) and four  $\text{Dy}^{\text{III}}$  ions (20  $\mu_B$ ) in a pure  $m_J = \pm 15/2 >$  ground state. The  $M$  versus  $H$  curves at 3 and 5 K also show similar increasing tendencies but do not overlap on the curve at 1.9 K, which can be attributed to significant magnetic anisotropy and/or the existence of low-lying excited states.



### 3.2.2. Dynamic Magnetic Properties of **Dy**<sub>2</sub> and **Dy**<sub>4</sub>

To investigate the dynamics of magnetization, alternating current (AC) susceptibility measurements were carried out with an oscillating field of 3.0 Oe. However, complex **Dy**<sub>2</sub> does not show any relaxation under zero dc field. It seems the magnetic interactions between the two Dy<sup>III</sup> ions are very weak and cannot suppress the fast relaxation of the complex. Field-dependent ac susceptibility measurements were carried out at 1.9 K with a frequency of 1000 Hz. As shown in Figure S12, the out-of-phase ac susceptibility ( $\chi''$ ) peak is detected around 1000 Oe, which should be the optimized dc field that can slow down the magnetic relaxation. Thus, we performed the ac susceptibility measurements under 1000 Oe dc field, and the temperature-dependent  $\chi''$  showed frequency-dependent peaks at low temperatures (Figure S13), indicating the slow relaxation of the magnetization. The frequency-dependent  $\chi''$  peaks shift to a higher frequency when raising the temperature, suggesting the thermal relaxation behaviors. For complex **Dy**<sub>4</sub>, the  $\chi''$  signals are observed under zero dc field but without peaks (Figure S14). This is probably related to the fast relaxation of QTM that shortcuts the relaxation of the magnetization.[62,63] This kind of relaxation can usually be suppressed by the application of dc field.[64,65] The optimized dc field was determined through the field-dependent ac susceptibility measurements (Figure S15), giving the optimized dc field of 500 Oe. After applying this dc field, frequency- and temperature-dependent  $\chi''$  peaks were observed in the ac measurements (Figures 3 and S16), indicative of the field-induced single-molecule magnetic property.

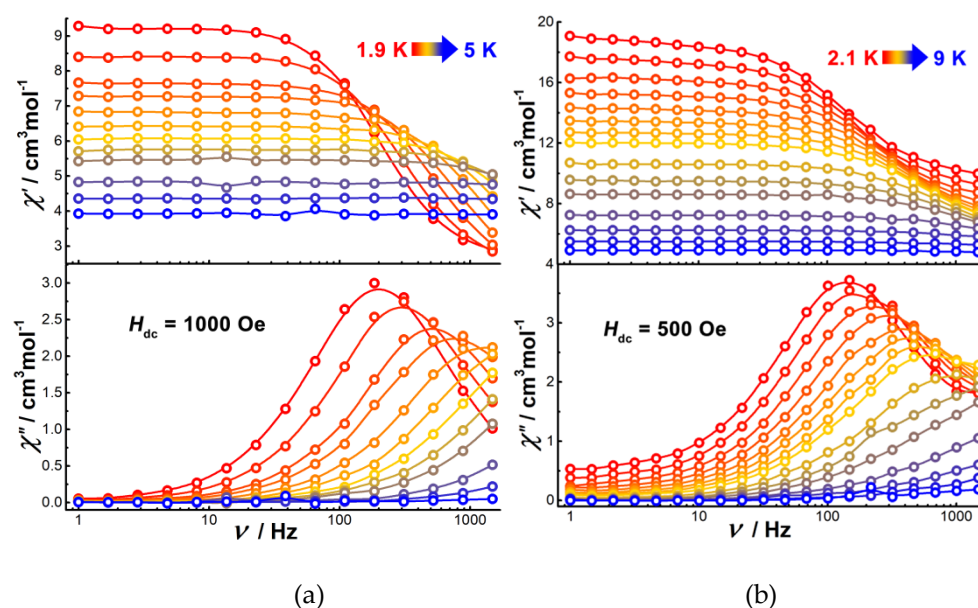


**Figure 3.** Frequency-dependent ac susceptibility of **Dy**<sub>2</sub> (a) and **Dy**<sub>4</sub> (b) under indicated dc field and temperature. The dots and solid lines are the data from ac measurements.

To explore the magnetic relaxation mechanics, Cole–Cole plots were represented as  $\chi''$  versus  $\chi'$  (Figure 4). For complexes **Dy**<sub>2</sub> and **Dy**<sub>4</sub>, the Cole–Cole plots show semi-circular profiles (Figure 4), suggesting the presence of a homogeneous relaxation process. Fitting the Cole–Cole plots with the CC-FIT2 program [66] using the Debye model [67] gives the temperature-dependent relaxation time. The relevant parameters of the fitting results are listed in Tables S5 and S6. Thereafter, we fit temperature-dependent relaxation by the following equation [68] to investigate the mechanics of the relaxation process:

$$\frac{1}{\tau_{\text{obs}}} = \frac{1}{\tau_{\text{QTM}}} + AH^4T + CT^n + \tau_0^{-1} \exp\left(-U_{\text{eff}}/T\right) \quad (1)$$

where  $1/\tau_{\text{QTM}}$ ,  $AH^4T$ ,  $CT^n$ , and  $\tau_0^{-1} \cdot \exp(-U_{\text{eff}}/T)$  represent quantum tunneling, direct, Raman, and Orbach relaxation processes, respectively. The relevant parameters obtained from the best fittings are listed in Table S7. Both complexes show Raman and Orbach relaxation processes with comparative Raman relaxation parameters (Table S7). The energy barriers of the two complexes are also comparative with  $U_{\text{eff}} = 17(4)$  K,  $\tau_0 = 4.3(3) \times 10^{-7}$  s,  $C = 144(5) \text{ s}^{-1} \cdot \text{K}^{-n}$ , and  $n = 3(0.3)$  for **Dy**<sub>2</sub>, and  $U_{\text{eff}} = 16(2)$  K,  $\tau_0 = 1.0(2) \times 10^{-3}$  s,  $C = 98(9) \text{ s}^{-1} \cdot \text{K}^{-n}$ , and  $n = 3(0.8)$  for **Dy**<sub>4</sub>.

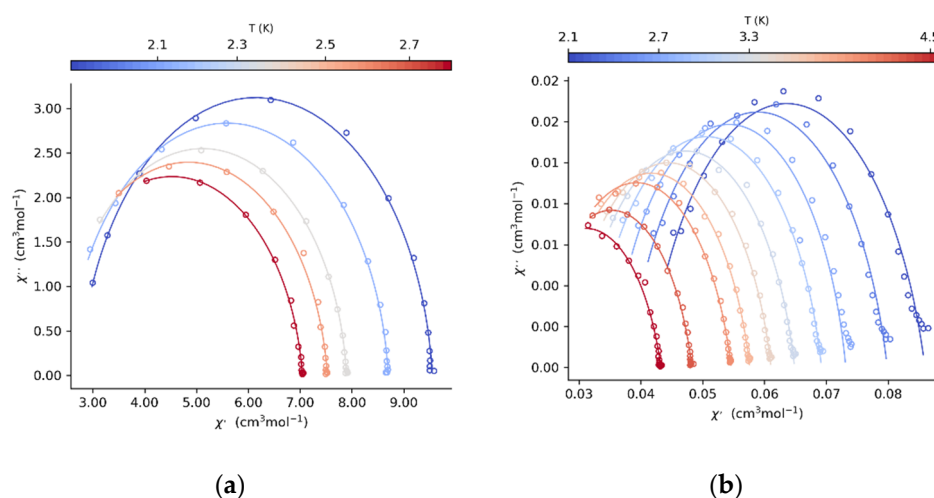


**Figure 4.** Cole-Cole plots for **Dy**<sub>2</sub> under 1000 Oe (a) and **Dy**<sub>4</sub> under 500 Oe (b) at the indicated temperature range. The solid lines represent the best fit.

The low energy barriers for both complexes are probably related to the poor axial ligand field of the **Dy**<sup>III</sup> ions. In complex **Dy**<sub>2</sub>, the **Dy**<sup>III</sup> ions reside in nine coordination environments with Dy-O bond length in the range of 2.37–2.46 Å and Dy-N bond of 2.50–2.57 Å, which indicate a relatively weak ligand field. For **Dy**<sub>4</sub>, the deprotonated hydroxymethyl groups give two shortest Dy-O bonds of 2.27 Å, which probably provides an axial ligand field that dominates the anisotropy of the complex. In order to investigate the anisotropies differences in the two complexes, we use the Magellan program [69] to calculate the anisotropy axes of each **Dy**<sup>III</sup> ion. The calculation is based on the X-ray structures and electrostatic model of the complexes, with the **Dy**<sup>III</sup> ions containing three positive charges and the coordinated O<sup>−</sup> and free Br<sup>−</sup> possessing one negative charge. For complex **Dy**<sub>2</sub>, the anisotropy axes of Dy1 and Dy2 are close to the cape-point of the capped square antiprism coordination polyhedron (Figure 5). For complex **Dy**<sub>4</sub>, the anisotropy axis of the Dy1 is parallel to the O1...O1' direction (Figure 5), which is beneficial from the shortest Dy-O bonds (2.27 Å) that provides a relatively stronger axial ligand field. Therefore, complex **Dy**<sub>4</sub> shows magnetic relaxation under zero field and a relatively slower relaxation time at low temperatures than that of **Dy**<sub>2</sub>.

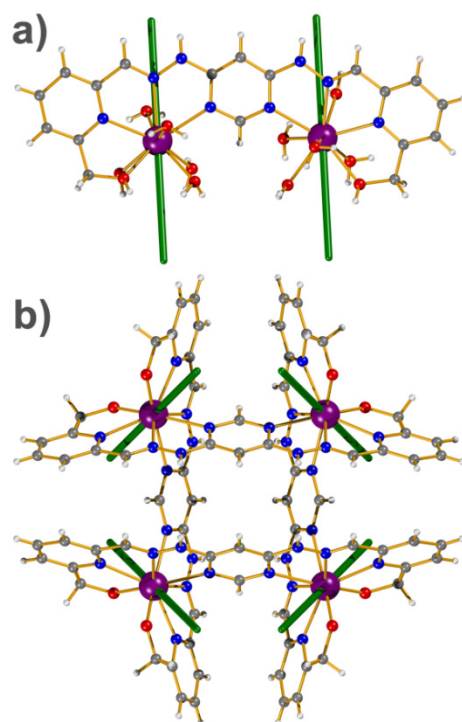


**Figure 5.** Orientations of the main magnetic axes of the ground state of **Dy<sub>2</sub>** (a) and **Dy<sub>4</sub>** (b) calculated based on the molecule structure.

#### 4. Conclusions

In conclusion, we synthesized a novel dicompartmental Schiff base ligand based on pyrimidine, by using which a dinuclear **Dy<sub>2</sub>** and tetranuclear **Dy<sub>4</sub>** grid were constructed. Due to the distinct coordination environments and topology in the two complexes, the magnetic relaxation of these complexes is different. In **Dy<sub>2</sub>**, the Dy<sup>III</sup> ions are in a relatively weak ligand field with relatively long coordination bonds; therefore, the complexes only show field-induced single-molecule magnet behavior. For complexes **Dy<sub>4</sub>**, the deprotonated ligand gives a pair of relatively short Dy–O bonds, resulting in the axial ligand field that slows down the relaxation. Therefore, complex **Dy<sub>4</sub>** shows relaxation under zero dc field and field-induced single-molecule magnetic behavior under 500 Oe dc field. Although the magnetic interactions in both complexes are weak and have no positive effect on the magnetic relaxation, the assembly of grid-type lanthanide clusters in the work provides an efficient strategy to regulate the topology of lanthanide ions. The next step will be focused on the enhancement of the magnetic coupling between lanthanide ions.

**Supplementary Materials:** The following are available online at <https://www.mdpi.com/article/10.3390/magnetochemistry9010004/s1>, Figure S1: Schematic drawings of the synthetic route of ligand **H<sub>2</sub>L**, Figure S2: <sup>1</sup>H-NMR spectrum of ligand **H<sub>2</sub>L** in DMSO-*d*<sub>6</sub>, Figures S3–S5: IR spectra of ligand **H<sub>2</sub>L**, complexes **Dy<sub>2</sub>** and **Dy<sub>4</sub>**, Figures S6 and S7: Packing models of complexes **Dy<sub>2</sub>** and **Dy<sub>4</sub>**, Figures S8 and S9: Coordination polyhedrons of Dy<sup>III</sup> ions in complexes **Dy<sub>2</sub>** and **Dy<sub>4</sub>**, Figures S10 and S11: Field-dependent molar magnetization of **Dy<sub>2</sub>** and **Dy<sub>4</sub>**, Figures S12–S16: Field- and temperature-dependent ac susceptibility of **Dy<sub>2</sub>** and **Dy<sub>4</sub>**, Figures S17 and S18: Plots of  $\tau$  vs.  $T^{-1}$  for **Dy<sub>2</sub>** and **Dy<sub>4</sub>**, Figures S19 and S20: Orientations of the main magnetic axes of the ground state of **Dy<sub>2</sub>** and **Dy<sub>4</sub>**, Table S1: Crystallographic data of **Dy<sub>2</sub>** and **Dy<sub>4</sub>**, Tables S2 and S3: Selected bond distances (Å) and angles (°) of **Dy<sub>2</sub>** and **Dy<sub>4</sub>**, Table S4: The *CSH*M values calculated by SHAPE 2.1 of Dy<sup>III</sup> ions in **Dy<sub>2</sub>** and **Dy<sub>4</sub>**, Tables S5 and S6: CC-Fit results for frequency-dependent ac susceptibility of **Dy<sub>2</sub>** and **Dy<sub>4</sub>**, Table S7: Parameters obtained from fitting the plots of the relaxation time  $\tau$  vs.  $1/T$  for **Dy<sub>2</sub>** and **Dy<sub>4</sub>**.



**Author Contributions:** Conceptualization, J.L.; Methodology, F.Z.; Software, D.L.; Formal analysis, F.Z. and X.G.; Investigation, J.L. and F.Z.; Data curation, X.G. and D.L.; Writing—original draft, J.L.; Writing—review & editing, D.L. and J.W.; Visualization, J.W.; Supervision, J.W.; Project administration, J.W.; Funding acquisition, J.W. All authors have read and agreed to the published version of the manuscript.

**Funding:** This research was funded by “National Natural Science Foundation of China, 22101229” and “The Open Funds of the State Key Laboratory of Rare Earth Resource Utilization, RERU2022021”.

**Data Availability Statement:** The data are available by corresponding authors.

**Acknowledgments:** We thank the National Natural Science Foundation of China (22101229) and the Open Funds of the State Key Laboratory of Rare Earth Resource Utilization (RERU2022021) for financial support.

**Conflicts of Interest:** The authors declare no conflict of interest.

## References

- Ishikawa, N.; Sugita, M.; Ishikawa, T.; Koshihara, S.-Y.; Kaizu, Y. Lanthanide Double-Decker Complexes Functioning as Magnets at the Single-Molecular Level. *J. Am. Chem. Soc.* **2003**, *125*, 8694–8695. [\[CrossRef\]](#) [\[PubMed\]](#)
- Feng, M.; Tong, M.L. Single Ion Magnets from 3d to 5f: Developments and Strategies. *Chem. Eur. J.* **2018**, *24*, 7574–7594. [\[CrossRef\]](#) [\[PubMed\]](#)
- Meng, Y.-S.; Jiang, S.-D.; Wang, B.-W.; Gao, S. Understanding the Magnetic Anisotropy toward Single-Ion Magnets. *Acc. Chem. Res.* **2016**, *49*, 2381–2389. [\[CrossRef\]](#) [\[PubMed\]](#)
- Sessoli, R.; Powell, A.K. Strategies towards single molecule magnets based on lanthanide ions. *Coord. Chem. Rev.* **2009**, *253*, 2328–2341. [\[CrossRef\]](#)
- Clemente-Juan, J.M.; Coronado, E.; Gaita-Arino, A. Magnetic polyoxometalates: From molecular magnetism to molecular spintronics and quantum computing. *Chem. Soc. Rev.* **2012**, *41*, 7464–7478. [\[CrossRef\]](#)
- Akiyoshi, R.; Zenno, H.; Sekine, Y.; Nakaya, M.; Akita, M.; Kosumi, D.; Lindoy, L.F.; Hayami, S. A Ferroelectric Metallomesogen Exhibiting Field-Induced Slow Magnetic Relaxation. *Chem. Eur. J.* **2022**, *28*, e202103367. [\[CrossRef\]](#)
- Sessoli, R.; Tsai, H.L.; Schake, A.R.; Wang, S.; Vincent, J.B.; Folting, K.; Gatteschi, D.; Christou, G.; Hendrickson, D.N. High-spin molecules: [Mn12O12(O2CR)16(H2O)4]. *J. Am. Chem. Soc.* **1993**, *115*, 1804–1816. [\[CrossRef\]](#)
- Gatteschi, D.; Caneschi, A.; Pardi, L.; Sessoli, R. Large Clusters of Metal Ions: The Transition from Molecular to Bulk Magnets. *Science* **1994**, *265*, 1054–1058. [\[CrossRef\]](#)
- Cosquer, G.; Shen, Y.; Almeida, M.; Yamashita, M. Conducting single-molecule magnet materials. *Dalton Trans.* **2018**, *47*, 7616–7627. [\[CrossRef\]](#)
- Dey, A.; Kalita, P.; Chandrasekhar, V. Lanthanide(III)-Based Single-Ion Magnets. *ACS Omega* **2018**, *3*, 9462–9475. [\[CrossRef\]](#)
- Guo, F.-S.; Bar, A.K.; Layfield, R.A. Main Group Chemistry at the Interface with Molecular Magnetism. *Chem. Rev.* **2019**, *119*, 8479–8505. [\[CrossRef\]](#) [\[PubMed\]](#)
- Zhu, Z.; Li, X.-L.; Liu, S.; Tang, J. External stimuli modulate the magnetic relaxation of lanthanide single-molecule magnets. *Inorganic Chemistry Frontiers* **2020**, *7*, 3315–3326. [\[CrossRef\]](#)
- Guo, F.-S.; Day, B.M.; Chen, Y.-C.; Tong, M.-L.; Mansikkamäki, A.; Layfield, R.A. Magnetic hysteresis up to 80 kelvin in a dysprosium metallocene single-molecule magnet. *Science* **2018**, *362*, 1400–1403. [\[CrossRef\]](#) [\[PubMed\]](#)
- Ishikawa, N.; Sugita, M.; Wernsdorfer, W. Quantum Tunneling of Magnetization in Lanthanide Single-Molecule Magnets: Bis(phthalocyaninato)terbium and Bis(phthalocyaninato)dysprosium Anions. *Angew. Chem. Int. Ed.* **2005**, *44*, 2931–2935. [\[CrossRef\]](#) [\[PubMed\]](#)
- Wernsdorfer, W.; Sessoli, R. Quantum Phase Interference and Parity Effects in Magnetic Molecular Clusters. *Science* **1999**, *284*, 133–135. [\[CrossRef\]](#)
- Gatteschi, D.; Sessoli, R. Quantum Tunneling of Magnetization and Related Phenomena in Molecular Materials. *Angew. Chem. Int. Ed.* **2003**, *42*, 268–297. [\[CrossRef\]](#)
- Guo, F.S.; Day, B.M.; Chen, Y.C.; Tong, M.L.; Mansikkamäki, A.; Layfield, R.A. A Dysprosium Metallocene Single-Molecule Magnet Functioning at the Axial Limit. *Angew. Chem. Int. Ed.* **2017**, *56*, 11445–11449. [\[CrossRef\]](#)
- Goodwin, C.A.P.; Ortu, F.; Reta, D.; Chilton, N.F.; Mills, D.P. Molecular magnetic hysteresis at 60 kelvin in dysprosocenium. *Nature* **2017**, *548*, 439–442. [\[CrossRef\]](#)
- Martynov, A.G.; Horii, Y.; Katoh, K.; Bian, Y.; Jiang, J.; Yamashita, M.; Gorbunova, Y.G. Rare-earth based tetrapyrrolic sandwiches: Chemistry, materials and applications. *Chem. Soc. Rev.* **2022**, *51*, 9262–9339. [\[CrossRef\]](#)
- Jiang, S.-D.; Wang, B.-W.; Su, G.; Wang, Z.-M.; Gao, S. A Mononuclear Dysprosium Complex Featuring Single-Molecule-Magnet Behavior. *Angew. Chem. Int. Ed.* **2010**, *49*, 7448–7451. [\[CrossRef\]](#)
- Wu, J.; Jung, J.; Zhang, P.; Zhang, H.; Tang, J.; Le Guennic, B. Cis-Trans Isomerism Modulates the Magnetic Relaxation of Dysprosium Single-Molecule Magnets. *Chem. Sci.* **2016**, *7*, 3632–3639. [\[CrossRef\]](#) [\[PubMed\]](#)

22. Wu, J.; Cador, O.; Li, X.-L.; Zhao, L.; Le Guennic, B.; Tang, J. Axial Ligand Field in D<sub>4d</sub> Coordination Symmetry: Magnetic Relaxation of Dy SMMs Perturbed by Counteranions. *Inorg. Chem.* **2017**, *56*, 11211–11219. [[CrossRef](#)] [[PubMed](#)]
23. Chen, Y.-C.; Liu, J.-L.; Ungur, L.; Liu, J.; Li, Q.-W.; Wang, L.-F.; Ni, Z.-P.; Chibotaru, L.F.; Chen, X.-M.; Tong, M.-L. Symmetry-Supported Magnetic Blocking at 20 K in Pentagonal Bipyramidal Dy(III) Single-Ion Magnets. *J. Am. Chem. Soc.* **2016**, *138*, 2829–2837. [[CrossRef](#)] [[PubMed](#)]
24. Liu, J.; Chen, Y.-C.; Liu, J.-L.; Vieru, V.; Ungur, L.; Jia, J.-H.; Chibotaru, L.F.; Lan, Y.; Wernsdorfer, W.; Gao, S.; et al. A Stable Pentagonal Bipyramidal Dy(III) Single-Ion Magnet with a Record Magnetization Reversal Barrier over 1000 K. *J. Am. Chem. Soc.* **2016**, *138*, 5441–5450. [[CrossRef](#)] [[PubMed](#)]
25. Yu, K.-X.; Kragoskow, J.G.C.; Ding, Y.-S.; Zhai, Y.-Q.; Reta, D.; Chilton, N.F.; Zheng, Y.-Z. Enhancing Magnetic Hysteresis in Single-Molecule Magnets by Ligand Functionalization. *Chem* **2020**, *6*, 1777–1793. [[CrossRef](#)]
26. Chen, Y.-C.; Tong, M.-L. Single-Molecule Magnets beyond a Single Lanthanide Ion: The Art of Coupling. *Chem. Sci.* **2022**, *13*, 8716–8726. [[CrossRef](#)] [[PubMed](#)]
27. Liu, F.; Krylov, D.S.; Spree, L.; Avdoshenko, S.M.; Samoylova, N.A.; Rosenkranz, M.; Kostanyan, A.; Greber, T.; Wolter, A.U.B.; Büchner, B.; et al. Single molecule magnet with an unpaired electron trapped between two lanthanide ions inside a fullerene. *Nat. Commun.* **2017**, *8*, 16098. [[CrossRef](#)]
28. Liu, F.; Velkos, G.; Krylov, D.S.; Spree, L.; Zalibera, M.; Ray, R.; Samoylova, N.A.; Chen, C.-H.; Rosenkranz, M.; Schiemenz, S.; et al. Air-stable redox-active nanomagnets with lanthanide spins radical-bridged by a metal–metal bond. *Nat. Commun.* **2019**, *10*, 571. [[CrossRef](#)]
29. Paschke, F.; Birk, T.; Enenkel, V.; Liu, F.; Romankov, V.; Dreiser, J.; Popov, A.A.; Fonin, M. Exceptionally High Blocking Temperature of 17 K in a Surface-Supported Molecular Magnet. *Adv Mater* **2021**, *33*, 2102844. [[CrossRef](#)]
30. Gould, C.A.; McClain, K.R.; Reta, D.; Kragoskow, J.G.C.; Marchiori, D.A.; Lachman, E.; Choi, E.-S.; Analytis, J.G.; Britt, R.D.; Chilton, N.F.; et al. Ultrahard magnetism from mixed-valence dilanthanide complexes with metal–metal bonding. *Science* **2022**, *375*, 198–202. [[CrossRef](#)]
31. Rinehart, J.D.; Fang, M.; Evans, W.J.; Long, J.R. Strong exchange and magnetic blocking in N<sub>2</sub> 32-radical-bridged lanthanide complexes. *Nat. Chem.* **2011**, *3*, 538–542. [[CrossRef](#)] [[PubMed](#)]
32. Demir, S.; Jeon, I.-R.; Long, J.R.; Harris, T.D. Radical ligand-containing single-molecule magnets. *Coord. Chem. Rev.* **2015**, *289–290*, 149–176. [[CrossRef](#)]
33. Demir, S.; Gonzalez, M.I.; Darago, L.E.; Evans, W.J.; Long, J.R. Giant coercivity and high magnetic blocking temperatures for N<sub>2</sub>3– radical-bridged dilanthanide complexes upon ligand dissociation. *Nat. Commun.* **2017**, *8*, 2144. [[CrossRef](#)] [[PubMed](#)]
34. Wang, J.; Li, Q.-W.; Wu, S.-G.; Chen, Y.-C.; Wan, R.-C.; Huang, G.-Z.; Liu, Y.; Liu, J.-L.; Reta, D.; Giansiracusa, M.J.; et al. Opening magnetic hysteresis by axial ferromagnetic coupling: From mono-decker to double-decker metallacrown. *Angew. Chem. Int. Ed.* **2021**, *60*, 5299–5306. [[CrossRef](#)] [[PubMed](#)]
35. Xiong, J.; Ding, H.-Y.; Meng, Y.-S.; Gao, C.; Zhang, X.-J.; Meng, Z.-S.; Zhang, Y.-Q.; Shi, W.; Wang, B.-W.; Gao, S. Hydroxide-bridged five-coordinate Dy(III) single-molecule magnet exhibiting the record thermal relaxation barrier of magnetization among lanthanide-only dimers. *Chem. Sci.* **2017**, *8*, 1288–1294. [[CrossRef](#)] [[PubMed](#)]
36. Wu, J.; Demeshko, S.; Dechert, S.; Meyer, F. Macrocyclic Based Dinuclear Dysprosium(III) Single Molecule Magnets with Local D<sub>5h</sub> Coordination Geometry. *Dalton Trans.* **2021**, *50*, 17573–17582. [[CrossRef](#)]
37. Lu, J.; Li, X.-L.; Jin, C.; Yu, Y.; Tang, J. Dysprosium-based linear helicate clusters: Syntheses, structures, and magnetism. *New J. Chem.* **2020**, *44*, 994–1000. [[CrossRef](#)]
38. Zhang, Y.; Ali, B.; Wu, J.; Guo, M.; Yu, Y.; Liu, Z.; Tang, J. Construction of Metallosupramolecular Coordination Complexes: From Lanthanide Helicates to Octahedral Cages Showing Single-Molecule Magnet Behavior. *Inorg. Chem.* **2019**, *58*, 3167–3174. [[CrossRef](#)]
39. Wu, J.; Li, X.-L.; Zhao, L.; Guo, M.; Tang, J. Enhancement of Magnetocaloric Effect through Fixation of Carbon Dioxide: Molecular Assembly from Ln<sub>4</sub> to Ln<sub>4</sub> Cluster Pairs. *Inorg. Chem.* **2017**, *56*, 4104–4111. [[CrossRef](#)]
40. Amlani, I.; Orlov, A.O.; Toth, G.; Bernstein, G.H.; Lent, C.S.; Snider, G.L. Digital Logic Gate Using Quantum-Dot Cellular Automata. *Science* **1999**, *284*, 289–291. [[CrossRef](#)]
41. Yang, Q.; Tang, J. Heterometallic grids: Synthetic strategies and recent advances. *Dalton Trans.* **2019**, *48*, 769–778. [[CrossRef](#)]
42. Wu, J.; Guo, M.; Li, X.-L.; Zhao, L.; Sun, Q.-F.; Layfield, R.; Tang, J. From Double-Shelled Grids to Supramolecular Frameworks. *Chem. Commun.* **2018**, *54*, 12097–12100. [[CrossRef](#)] [[PubMed](#)]
43. Wu, J.; Zhao, L.; Guo, M.; Tang, J. Constructing supramolecular grids: From 4f square to 3d-4f grid. *Chem. Commun.* **2015**, *51*, 17317–17320. [[CrossRef](#)] [[PubMed](#)]
44. Wu, J.; Zhao, L.; Zhang, L.; Li, X.-L.; Guo, M.; Tang, J. Metallosupramolecular Coordination Complexes: The Design of Heterometallic 3d–4f Gridlike Structures. *Inorg. Chem.* **2016**, *55*, 5514–5519. [[CrossRef](#)] [[PubMed](#)]
45. Wu, J.; Zhao, L.; Zhang, L.; Li, X.-L.; Guo, M.; Powell, A.K.; Tang, J. Macroscopic Hexagonal Tubes of 3d–4f Metalloclusters. *Angew. Chem. Int. Ed.* **2016**, *55*, 15574–15578. [[CrossRef](#)] [[PubMed](#)]
46. Wu, J.; Li, X.-L.; Guo, M.; Zhao, L.; Zhang, Y.; Tang, J. Realization of toroidal magnetic moments in heterometallic 3d-4f metalloclusters. *Chem. Commun.* **2018**, *54*, 1065–1068. [[CrossRef](#)] [[PubMed](#)]
47. Wu, J.; Liu, D.; Yang, Q.; Ge, Y.; Tang, J.; Qi, Z. Magnetic investigation in di- and tetranuclear lanthanide complexes. *New J. Chem.* **2021**, *45*, 2200–2207. [[CrossRef](#)]

48. Alam, M.S.; Strömsdörfer, S.; Dremov, V.; Müller, P.; Kortus, J.; Ruben, M.; Lehn, J.-M. Addressing the Metal Centers of  $[2 \times 2]$  CoII<sub>4</sub> Grid-Type Complexes by STM/STS. *Angew. Chem. Int. Ed.* **2005**, *44*, 7896–7900. [\[CrossRef\]](#)
49. Barboiu, M.; Stadler, A.-M.; Lehn, J.-M. Controlled Folding, Motional, and Constitutional Dynamic Processes of Polyheterocyclic Molecular Strands. *Angew. Chem. Int. Ed.* **2016**, *55*, 4130–4154. [\[CrossRef\]](#)
50. Bassani, D.M.; Lehn, J.-M.; Fromm, K.; Fenske, D. Toposelective and Chiroselective Self-Assembly of  $[2 \times 2]$  Grid-Type Inorganic Arrays Containing Different Octahedral Metallic Centers. *Angew. Chem. Int. Ed.* **1998**, *37*, 2364–2367. [\[CrossRef\]](#)
51. Wang, Y.-T.; Li, S.-T.; Wu, S.-Q.; Cui, A.-L.; Shen, D.-Z.; Kou, H.-Z. Spin Transitions in Fe(II) Metallogrids Modulated by Substituents, Counteranions, and Solvents. *J. Am. Chem. Soc.* **2013**, *135*, 5942–5945. [\[CrossRef\]](#)
52. Dhers, S.; Mondal, A.; Aguilà, D.; Ramírez, J.; Vela, S.; Dechambenoit, P.; Rouzières, M.; Nitschke, J.R.; Clérac, R.; Lehn, J.-M. Spin State Chemistry: Modulation of Ligand pK<sub>a</sub> by Spin State Switching in a  $[2 \times 2]$  Iron(II) Grid-Type Complex. *J. Am. Chem. Soc.* **2018**, *140*, 8218–8227. [\[CrossRef\]](#) [\[PubMed\]](#)
53. Li, X.-L.; Wu, J.; Zhao, L.; Shi, W.; Cheng, P.; Tang, J. End-to-end azido-pinned interlocking lanthanide squares. *Chem. Commun.* **2017**, *53*, 3026–3029. [\[CrossRef\]](#) [\[PubMed\]](#)
54. Uppadine, L.H.; Gisselbrecht, J.-P.; Kyritsakas, N.; Nättinen, K.; Rissanen, K.; Lehn, J.-M. Mixed-Valence, Mixed-Spin-State, and Heterometallic  $[2 \times 2]$  Grid-type Arrays Based on Heteroditopic Hydrazone Ligands: Synthesis and Electrochemical Features. *Chem. Eur. J.* **2005**, *11*, 2549–2565. [\[CrossRef\]](#) [\[PubMed\]](#)
55. Join, B.; Möller, K.; Ziebart, C.; Schröder, K.; Gördes, D.; Thurow, K.; Spannenberg, A.; Junge, K.; Beller, M. Selective Iron-Catalyzed Oxidation of Benzylic and Allylic Alcohols. *Adv. Synth. Catal.* **2011**, *353*, 3023–3030. [\[CrossRef\]](#)
56. Dolomanov, O.V.; Bourhis, L.J.; Gildea, R.J.; Howard, J.A.K.; Puschmann, H. OLEX2: A complete structure solution, refinement and analysis program. *J. Appl. Crystallogr.* **2009**, *42*, 339–341. [\[CrossRef\]](#)
57. Sheldrick, G. SHELXT - Integrated space-group and crystal-structure determination. *Acta Crystallographica Section A* **2015**, *71*, 3–8. [\[CrossRef\]](#)
58. Sheldrick, G. Crystal structure refinement with SHELXL. *Acta Crystallographica Section C* **2015**, *71*, 3–8. [\[CrossRef\]](#)
59. Boudreaux, E.A.; Mulay, L.N. *Theory and Applications of Molecular Paramagnetism*; John Wiley & Sons: New York, NY, USA, 1976.
60. Casanova, D.; Alemany, P.; Bofill, J.M.; Alvarez, S. Shape and Symmetry of Heptacoordinate Transition-Metal Complexes: Structural Trends. *Chem. Eur. J.* **2003**, *9*, 1281–1295. [\[CrossRef\]](#)
61. Casanova, D.; Llunell, M.; Alemany, P.; Alvarez, S. The Rich Stereochemistry of Eight-Vertex Polyhedra: A Continuous Shape Measures Study. *Chem. Eur. J.* **2005**, *11*, 1479–1494. [\[CrossRef\]](#)
62. Acharya, J.; Ahmed, N.; Flores-Gonzalez, J.; Kumar, P.; Pointillart, F.; Cador, O.; Singh, S.K.; Chandrasekhar, V. Slow Magnetic Relaxation in a Homo Dinuclear Dy(III) Complex in a Pentagonal Bipyramidal Geometry. *Dalton Trans.* **2020**, *49*, 13110–13122. [\[CrossRef\]](#)
63. Yang, H.; Liu, S.-S.; Meng, Y.-S.; Zhang, Y.-Q.; Pu, L.; Wang, X.; Lin, S. Four mononuclear dysprosium complexes with neutral Schiff-base ligands: Syntheses, crystal structures and slow magnetic relaxation behavior. *Dalton Trans.* **2022**, *51*, 1415–1422. [\[CrossRef\]](#) [\[PubMed\]](#)
64. Yang, Q.; Wang, G.-L.; Zhang, Y.-Q.; Tang, J. Self-assembly of fish-bone and grid-like CoII-based single-molecule magnets using dihydrazone ligands with NNN and NNO pockets. *Dalton Trans.* **2022**, *51*, 13928–13937. [\[CrossRef\]](#) [\[PubMed\]](#)
65. Ashebr, T.G.; Li, X.-L.; Zhao, C.; Yang, Q.; Tang, J. Bis-pyrazolone-based dysprosium(III) complexes: Zero-field single-molecule magnet behavior in the  $[2 \times 2]$  grid DyIII<sub>4</sub> cluster. *CrystEngComm* **2022**, *24*, 6688–6695. [\[CrossRef\]](#)
66. Reta, D.; Chilton, N.F. Uncertainty estimates for magnetic relaxation times and magnetic relaxation parameters. *PCCP* **2019**, *21*, 23567–23575. [\[CrossRef\]](#) [\[PubMed\]](#)
67. Debye, P. Einige Bemerkungen zur Magnetisierung bei tiefer Temperatur. *Ann. Phys.* **1926**, *386*, 1154–1160. [\[CrossRef\]](#)
68. Demir, S.; Zadrozny, J.M.; Long, J.R. Large Spin-Relaxation Barriers for the Low-Symmetry Organolanthanide Complexes [Cp\*<sub>2</sub>Ln(BPh<sub>4</sub>)] (Cp\* = pentamethylcyclopentadienyl; Ln = Tb, Dy). *Chem. Eur. J.* **2014**, *20*, 9524–9529. [\[CrossRef\]](#)
69. Chilton, N.F.; Collison, D.; McInnes, E.J.L.; Winpenny, R.E.P.; Soncini, A. An electrostatic model for the determination of magnetic anisotropy in dysprosium complexes. *Nat. Commun.* **2013**, *4*, 2551. [\[CrossRef\]](#)

**Disclaimer/Publisher's Note:** The statements, opinions and data contained in all publications are solely those of the individual author(s) and contributor(s) and not of MDPI and/or the editor(s). MDPI and/or the editor(s) disclaim responsibility for any injury to people or property resulting from any ideas, methods, instructions or products referred to in the content.